Growth of conjugated oligomer thin films studied by atomic-force microscopy

F. Biscarini
Istituto di Spettroscopia Molecolare, Consiglio Nazionale delle Ricerche, Via Gobetti 101, 40129 Bologna, Italy and Istituto di Chimica e Tecnologia dei Materiali e dei Componenti per l'Elettronica (LAMEL), Consiglio Nazionale delle Ricerche, Via Gobetti 101, 40129 Bologna, Italy

R. Zamboni and P. Samorí*
Istituto di Spettroscopia Molecolare, Consiglio Nazionale delle Ricerche, Via Gobetti 101, 40129 Bologna, Italy

P. Ostoja
Istituto di Chimica e Tecnologia dei Materiali e dei Componenti per l'Elettronica (LAMEL), Consiglio Nazionale delle Ricerche Via Gobetti 101, 40129 Bologna, Italy

C. Taliani
Istituto di Spettroscopia Molecolare, Consiglio Nazionale delle Ricerche, Via Gobetti 101, 40129 Bologna, Italy
(Received 23 June 1995)

We present a quantitative investigation by atomic-force microscopy of the growth of an organic thin film made of sexithienyl evaporated on mica in high vacuum. Different forms of aggregation in sexithienyl thin films are induced upon a systematic increase in the temperature of the substrate during the evaporation. For temperatures up to 150 °C, the films consist of tightly packed grains whose size increases with temperature according to an Arrhenius behavior with ~0.36 eV activation energy. The χ-square grain-size distribution suggests that growth rate is controlled by diffusion. This mechanism is supported by a simple model calculation of the van der Waals interaction between a single $T6$ molecule and a (100) $T6$ surface, that yields energy barriers to translation and rotation of the molecule equal to 0.3 and 0.5 eV, respectively. At 200 °C the film undergoes a morphological change to a lamellar structure and extended microcrystalline structures appear at higher temperatures. The presence of preferential directions suggests that orientational ordering is induced by the mica substrate. The possibility of obtaining ordered aggregates by a suitable choice of substrate and temperature during evaporation has relevance towards the realization of molecular devices with anisotropic properties.

I. INTRODUCTION

There is a growing interest in π-conjugated organic systems as the active layer in devices such as field-effect transistors[1] (FET) and light-emitting diodes[2] (LED). The transport phenomena in these molecular devices depends on the interplay between electronic structure and order in the molecular assembly. Charge injection, mobility, and recombination will depend, among other parameters, on molecular packing, extent of grain boundaries, and roughness of the interface with the electrodes.

Among several electroactive species, large oligothiophenes (four to six units) are suitable prototypes for polythiophene, since they possess a closely related electronic structure[3] and, furthermore, can give rise to self-ordered aggregates.[4–9] These molecules can be obtained as a pure material and processed as thin films in high-vacuum (HV) conditions.

The present work focuses on α-sexithienyl ($T6$), whose molecular structure is shown in Fig. 1. $T6$ crystals belong to the monoclinic $P21/n$ space group,[5] and some of the original crystal structure is preserved in $T6$ films depending upon the sample preparation conditions. In particular, the temperature of the substrate during evaporation,[7] the rate of evaporation,[8,9] and the film thickness[8] are important parameters. For example, films evaporated on silicon at rates 0.2–10 Å/s exhibit x-ray-diffraction (XRD) peaks corresponding to a 2.30-nm interlayer spacing.[1(d)] Larger evaporation rates (10–100 Å/s) yield polycrystalline aggregates with a bimodal distribution of molecular orientations, with the long molecular axis either perpendicular or lying flat on the surface.[6,7] The smallest rates (0.2–1 Å/min) achieved in UHV yield films with molecules standing perpendicular to the surface.[8,9] The nature of the substrate and chemical substituent groups can completely change the order of the molecular aggregate, as shown by helium scattering[10] and scanning tunneling microscopy.[11]

Although there has been a considerable effort towards the elucidation of $T6$ crystal structure, the study of the morphology of $T6$ aggregates and its correlation with transport and optical properties of interest has started more recently.[7,9] A combined investigation with XRD, UV-visible spectroscopy, and scanning electron microscopy has linked polymorphism to the FET mobility and anisotropy of the conductivity in $T6$ film prepared at different substrate temperatures.[7] The sensitivity of the $T6$ luminescence quantum yield to different sample preparations has been related to differences in morphology.[3(d)] Furthermore, while photoinduced absorption is similar to that measured on disordered polythiophene,[12] Stark spectroscopy of ordered $T6$ films on silicon shows the presence of charge-transfer excitons in the UV-visible region with preferential *e-h* dissociation

 ©1995 The American Physical Society

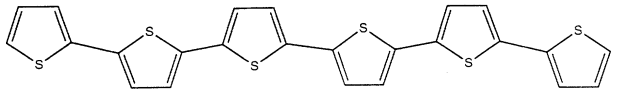

FIG. 1. Structure of α-sexithienyl.

along the stack of molecular layers.[13] These observations suggest that charges are generated at a molecular site and that long-range transport takes place by intermolecular hopping.[14]

Preparation of oligomer thin films with well-defined structural features is therefore crucial both for fundamental studies and for realization of optimal molecular devices, but more systematic effort along this direction has to be undertaken.

In this work we have used atomic-force microscopy (AFM) to study the growth of *T*6 films as a function of the temperature of the substrate during the deposition. The present investigation concerns films $\sim$100 nm thick, which is comparable to the thickness used for LED's. Beyond the morphological changes, the main outcome of the present study is to show how AFM can be used to measure the growth activation energy of an organic thin film. Insights into the nature and strength of intermolecular interactions are drawn from the distribution of particle sizes.

II. EXPERIMENT

A. Materials

*T*6 was synthesized by coupling via Grignard reagents catalyzed by [1,2-bis(diphenylphosphino)ethane] nickel chloride,[15] and after high-vacuum sublimation it appears as a bright orange crystalline powder. The substrate is freshly cleaved ruby mica (Plano WPlannet GmbH, Marburg, Germany), which is a convenient model substrate due to its small corrugation.

B. Sample preparation

*T*6 films are prepared by high-vacuum (5×10^{-6}–10^{-7} mbar) evaporation of the purified material from a Knudsen cell in a modified commercial apparatus (Edwards Auto306). The configuration of the system is constant for all samples, with the substrate placed 10 cm above the quartz crucible containing *T*6, and normal to its axis. The typical heating ramp for the crucible consists of a fast rise up to 200 °C, a plateau to purge possible traces of contaminants and lower mass oligomers, then a final rise to 260–300 °C during which sublimation takes place. The deposition rate is monitored by a quartz oscillator placed beside the substrate, and it is on the order of 0.2–1 Å/s. For comparison with earlier works, this value is at least one order of magnitude larger than effusion rates in UHV,[8,9] and one to two orders of magnitude smaller than flash sublimation.[6,7] All samples are normalized to a nominal 60-nm film thickness. Film thickness is well above a few monolayers (1 ML $\sim$ 2.5 nm) as is apparent from the yellow-orange color of the film. Color and transparency depend on substrate temperature and films prepared on a substrate above 200 °C appear opaque, as the result of increased scattering. We have performed *ex situ* AFM imaging of edges between mica and *T*6 film in masked samples, measuring a difference of 100 nm between the average height of the organic film and mica. Furthermore, on other samples, we have scraped organic material away by repeated scanning at high force on small areas, obtaining pits 70–100 nm deep. Similar experiments on bare ruby mica after the same thermal treatment did not show any removal of material. Thus, we estimate that the actual film thickness is 30–50 % larger than its nominal value.

C. Atomic-force microscopy

AFM topographical images have been obtained with a commercial instrument (Topometrix TMX2010) in contact mode using 1–10-Hz scan rates. Since the organic thin film is soft, particular care has to be taken in order to avoid damage to the sample. Soft cantilevers (spring constant 0.03–0.06 N/m) produce neither damage nor change in the apparent particle height on the 100-nm scale, as we observed after repeated scanning at the highest load force on small areas. Displacement of film material has been observed when a high force was used on films deposited on mica substrate at 22 °C, and extensive damage can be produced by stiffer levers (17–64 N/m). In order to work with a setpoint force of 0.5–5 nN and to minimize the contact area, relative humidity was kept between 20% and 30% by flushing dry nitrogen in the measurement chamber, resulting in an improvement of the quality of the images.

III. RESULTS AND DISCUSSION

A. Film morphology

Figure 2 shows typical 10 μm$\times$10 μm images of samples prepared at substrate temperatures from 22 °C up to 150 °C. The film consists of grains whose size increases consistently with temperature. The sequence in Fig. 2 suggests that the morphology is substantially the same and that the same mechanism governs the growth in this temperature range. The similarity at different temperatures can be seen by rescaling the image size according to the respective grain size (Fig. 3). Aggregation of tightly packed rounded grains is clearly visible in all samples at 22 °C and 100 °C [Figs. 3(a) and 3(b)], in qualitative agreement with observations by scanning electron microscopy on *T*6 film on Si.[7] From the density of voids in the sequence in Fig. 3 there is an apparent decrease in the film density. At 150 °C the contacts between adjacent grains become extended, and a network of large grains joined by convex necks is formed [Figs. 2(d) and 3(c)]. It is known that minimization of the surface energy at a contact point drives neck formation.[16] This process takes place through migration of material at the surface that eventually yields coalescence of smaller particles. The smoother appearance of the grains and the mirror crevices resolved within the grains at 150 °C seem to support this mechanism. The rounded shape of grains in Figs. 3(a) and 3(b)

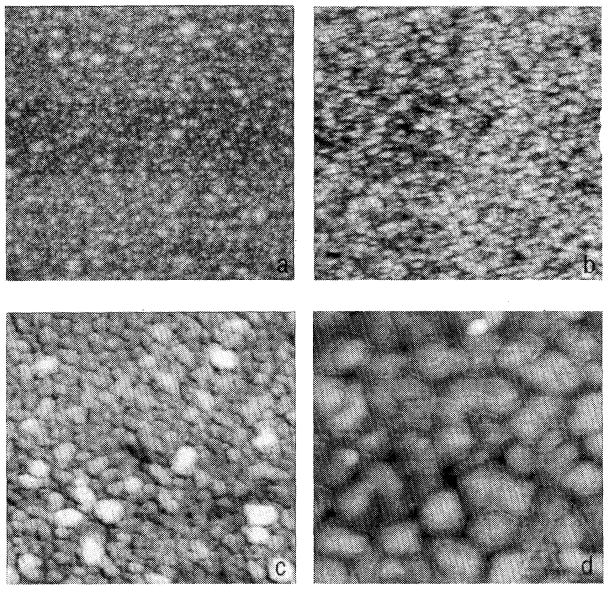

FIG. 2. 10 μm$\times$10 μm unfiltered topographical images of $T6$ films evaporated on mica. Substrate temperatures are (a) 22 °C (vertical scale 0–102 nm, scan rate 5 Hz); (b) 75 °C (vertical scale 0–130 nm, scan rate 3 Hz); (c) 100 °C (vertical scale 0–102 nm, scan rate 5 Hz); (d) 150 °C (vertical scale 0–132 nm, scan rate 10 Hz). Resolution is 400 pixels per line.

suggests that no particular order is attained at lower temperatures. In contrast, close inspection reveals sharp angles between the platelets around the void channels in the sample at 150 °C [Fig. 3(c)]. Since structural order increases with the mobility of single molecules or small clusters, we expect that the size of ordered domains within a grain should increase as well. The appearance of an ordered structure in the direction perpendicular to the surface would result in XRD reflections from (00l) lattice planes,[6,7] and anisotropy in transport[7,13] and optical[3(c),7,9,16] properties. From line profiles across the smoother grains in images of 150 °C samples, we were able to resolve 2–3-nm-high (and integer multiple) steps between ~200-nm-wide flat terraces. This is consistent with the 2.2-nm spacing between monolayer lattice planes measured by diffraction techniques.[4–7] These observations suggest that memory of a layer-by-layer growth is maintained in the three-dimensional growth, even after the first nucleation process is completed.[8] The scarce occurrence of steps can be explained either in terms of intrinsic disorder at the grain boundaries, or as the result of smearing due to the imaging technique (for example, the effects of a large tip radius of curvature or excessive friction force).

At 200 °C substrate temperature, the film morphology undergoes a phase transition from grains to oriented lamellae with sharp edges separated by large voids [Fig. 4(a)]. The crystallites are strongly anisotropic and their axes align according to preferential directions [shown in Fig. 4(a)] forming 30°, 60°, 90° and 120° angles, approximately. These values match the angles between crystallographic directions observed on freshly cleaved ruby mica with a polarizing microscope. Since the extinction axes coincide with the a and b vectors of the mica orthorhombic lattice [the cleavage layer is the (001) plane], then one can assign to the [010], [$\bar{1}$10], [110] directions the most frequently encountered basal-plane edges on mica. It is well known that isolated molecules adsorb preferentially at step edges, because of strong electrostatic fields present there. Therefore, stable nuclei may form along the cleavage-plane edges even at high temperature, and together with the intrinsic anisotropy of $T6$, induce preferential orientations in the film. This observation indicates that a suitable choice of substrate or surface treatment could be a useful route to control the anisotropy of $T6$ aggregates.

The transition is accompanied by a change in the film corrugation: the average height of grains ranges on the ~100-nm vertical scale, while that of lamellae ranges three to nine times larger. The modest but significative decrease in the packing density suggests a phase transition being of weak first order or second order. The nature of the 200 °C phase is not known yet, although the lamellae resemble those of a smectic mesophase. In this context, a nematic phase stable from 305–312 °C at 1 atm has been identified.[17]

At 220 °C, crystalline aggregates whose size extends to several tens of square micrometers are formed [Fig. 4(b)] and the same preferred crystal directions as in Fig. 4(a) are present. Despite the different morphology of the lamellar aggregate, a similar trend is observed by XRD of $T6$ films on silicon where a sequence of transitions, from an α phase (stable at 22 °C and above) to a γ phase (at 190 °C), and then to a δ phase (at 220 °C and above)

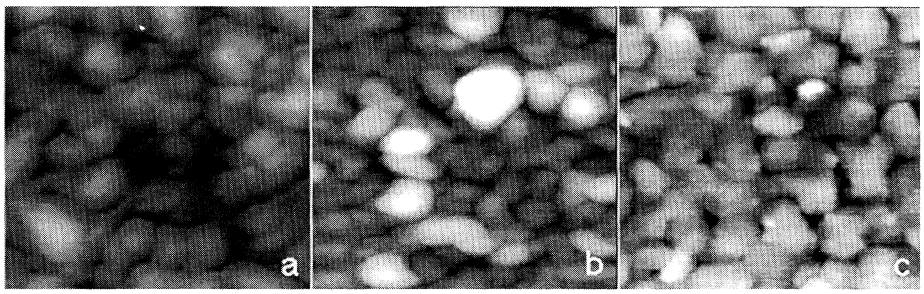

FIG. 3. Unfiltered topographical images of $T6$ films showing the similar morphology for samples evaporated on mica at (a) 22 °C (1-μm$\times$1-μm zoom from a 2-μm$\times$2-μm image); (b) 100 °C (5 μm$\times$5 μm); (c) 150 °C (10 μm$\times$10 μm).

occurs.[7] Each phase is characterized by the stacking of monolayers parallel to the substrate and by an increasing interlayer spacing.

The potential to produce a highly ordered two-dimensional system has interesting implications in terms of anisotropy in charge and exciton mobility, optical polarization, and emission wavelength. Our results suggest that a crystalline substrate possibly favors growth along preferential directions, provided favorable conditions are present for the molecule to find the most suitable arrangement (such as low deposition rates or high temperature). However, it should be noticed that the gain in order displayed in Fig. 4 is accompanied by a loss of compactness that would cause leakage and short circuits in the operation of a molecular device. The increasing density of pinholes could explain the spatial inhomogeneities and the smaller value of the FET conductivity observed in samples deposited at high substrate temperatures.[7]

FIG. 4. 10-μm$\times$10-μm topographical images of $T6$ films evaporated on mica at (a) 200 °C (scale bar 0–346 nm, scan rate 5 Hz) and (b) 220 °C (scale bar 0–880 nm, scan rate 5 Hz). Solid lines show the preferred orientation of the crystallites. Labels correspond to possible mica lattice directions. The contrast is enhanced by equalization of the histogram.

B. Data analysis

We have studied the evolution of the grain size with the substrate temperature by measuring the projection of grains onto the surface plane. Because of the compact film morphology, grains are selected individually following the necks and major crevices around them (Fig. 5). Each particle is isolated by drawing manually a one-pixel rough boundary with a black line so that the boundary coincides with the lowest feature in the color scale. Then, thresholding is done within the manually drawn boundary at a slightly lighter color, so that there is not necessarily alignment between the thresholding and the manually drawn data. Thresholding usually matches or slightly underestimates the grain area leaving the boundaries out. However, we have chosen to work with the data from local thresholding to reduce the arbitrariness and difficulty of the operator's judgment in following the optimal profile. Finally, pixel counting is performed on the area obtained by thresholding at low height. These operations are performed with NIH-IMAGE software (National Institutes of Health, Bethesda, Maryland). An example is shown in Fig. 5, where 16 particles (circled by white lines) are selected with this procedure. Particles touching the image edges are discarded. For each substrate temperature, the statistics are built out of 400–500 particles, taken from 10–20 images whose sizes range between five and ten times the typical grain diameter. Albeit crude and time-consuming, this approach leads to more reliable distributions than a standard thresholding procedure performed on the entire image. We have decided not to perform the statistics on diameters measured from line scans, as is often done,[18] because of the shape anisotropy and irregularity of the edges.

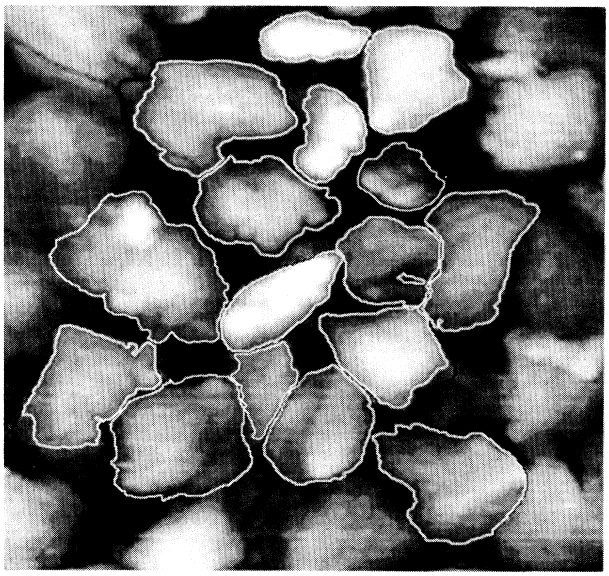

FIG. 5. Sampling of projections for the statistics of grain size. Solid black lines follow the major crevices and necks around each grain; white line is the contour selected by thresholding. The area is calculated from pixel-by-pixel counting within the white line.

One of the crucial problems in undertaking a statistical study with a local microscopy is to select images that are representative of the sample features. In this study, we have done this by the comparison of the power spectra (i.e., the Fourier transform of the height autocorrelation function).[19] In our implementation, a trend removal is performed on each image by subtraction of the best fit plane from raw data, and no filtering is applied. Then the power spectrum is calculated via fast Fourier transform of the topographical profile along the fast scan direction (x). As an example, in Fig. 6 we show the good reproducibility of the power spectra of 10-μm×10-μm images taken from three different areas of the same sample (a), and from two different areas of two independent samples prepared at the same substrate temperature (b). Comparison of power spectra from 20 to 50 images allows us to establish a sufficient number of "typical images" and to reject images with anomalous power spectra. The fraction of images discarded with this procedure ranges between 5% and 20% of the total images acquired for each sample. These anomalies manifest usually as large aliasing, which appears to be related to the presence of local inhomogeneities in the spatial features (such as the presence of protruding grains or large cavities). Therefore, they are most frequently encountered on scan lengths where a small (10–30) number of grains are imaged. Concerning roughness, a detailed analysis on the spectral behavior against the spatial frequency as well its dependence on the temperature will be reported soon. Here it suffices to say that the power-law decay reveals the self-affine nature of these surfaces, typical of systems grown in conditions of nonequilibrium. The low-frequency plateau denotes the absence of long-range correlation for large spatial features, and its onset (which is related to some characteristic grain size) shifts consistently to lower spatial frequencies as the substrate temperature increases, in agreement with the observed increase in grain size. Finally, a few considerations are required about the measurement of the grain lateral size and the error introduced by neglecting the tip envelope.[20] Since tip effects are important when sample features are smaller or comparable to the tip radius of curvature, the error should be more significant for samples prepared at 22 °C substrate temperature, where particle diameters are about three times the radius of curvature of a standard pyramidal tip (20–50 nm), and it should decrease for samples prepared at higher substrate temperatures. The apparent average height of the film is also comparable (60–100 nm) to the tip radius of curvature. If individual grains were imaged, the apparent diameter would be 70% larger than the actual one for $T_{\text{mica}}=22$ °C, and 10% for $T_{\text{mica}}=150$ °C. However, these estimates are excessively conservative since the tip cannot penetrate deep into the crevices due to the compactness of the film. Thus, grain boundaries should be mapped accurately, except for smaller particles embedded in the interstices that cannot be reached by the tip.

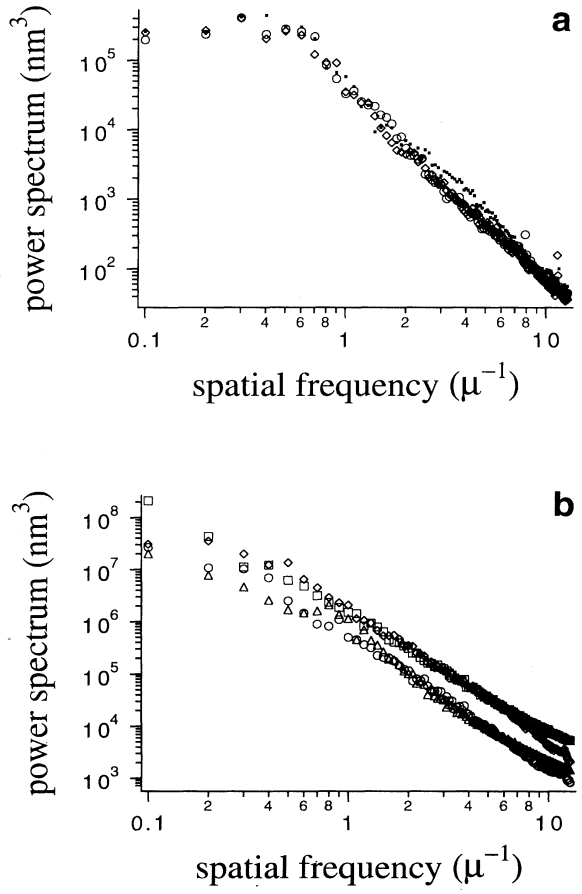

FIG. 6. Power spectrum vs spatial frequency calculated from 10-μm×10-μm unfiltered AFM images: (a) comparison between spectra from images taken on different areas a few millimeters apart on the same sample ($T_{\text{mica}}=150$ °C); (b) comparison between spectra from images taken from two samples (circles and diamonds, triangles and squares, respectively) prepared at the same temperature ($T_{\text{mica}}=200$ °C).

The histograms in Fig. 7 show that the distributions spread out and their mode shifts to higher particle sizes as the substrate temperature increases. In Fig. 8(a) the temperature dependence of the average grain size $\langle A \rangle$ exhibits a clear Arrhenius-type behavior. The error bar of each distribution is calculated as the average absolute deviation $\Delta A \approx (1/N)\sum_i |A_i - \langle A \rangle|$, where N is the number of particles in the data set.[21] Weighted least-square fitting of the logarithm of the average size versus inverse temperatures provides an excellent correlation coefficient (0.985 for seven data points, T from 22 to 150 °C), and an activation energy $E_A=0.36\pm0.04$ eV. The transition from grains to lamellae around 200 °C occurs without a large discontinuity in the average area. Including the 200 °C average area in the fit decreases the correlation coefficient to 0.932, but without other significant differences. The analysis of the higher moments, i.e., $\langle A^n \rangle$, allows us to characterize the relevant distribution. From Fig. 8(b), it appears that σ, the standard deviation of the area (related to the second moment), is a linear function of the mean area $\langle A \rangle$. This feature is typical of a χ^2 distribution, indicating that the area is determined by a set of independent stochastic variables, each with a Gaussian distribution.[22,23] Such distributions are characterized by the mean and a number

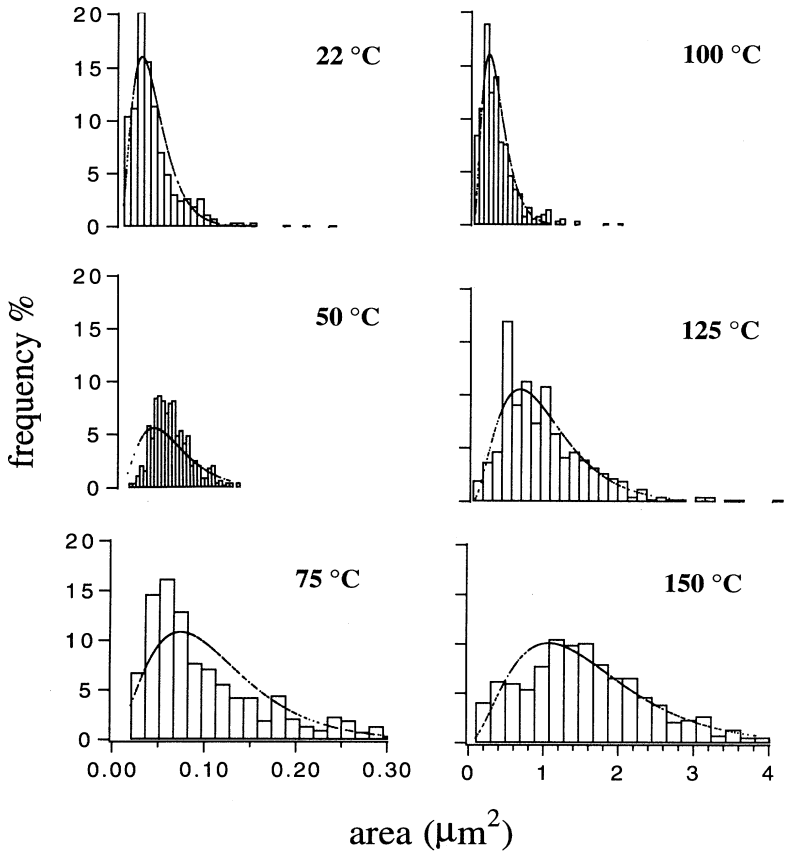

FIG. 7. Evolution of the distribution of the grain size with temperature. The left axis shows the percentage frequency, calculated from 525 (22 °C), 425 (50 °C), 519 (75 °C), 470 (100 °C), 405 (125 °C), and 526 (150 °C) individual particles, respectively. Dotted lines are Pearson type-III distribution (3.1) multiplied by the respective bin size to yield a probability. The average area from each sample is taken as the parameter characterizing the distribution.

p, representing the number of independent variables. In this case, p represents the physical dimensions active in the growth process. Since the standard deviation is related to the mean by $\sigma=(1/\sqrt{p}\,)\langle A\rangle$,[22] the value for p is extracted from the slope of the best fit curve in Fig. 8(b). The fitting yields $p=3.2\pm0.3$ (correlation coefficient 0.993 for seven points), while log-log plot fitting yields $p=2.7\pm0.4$ (correlation coefficient 0.985). We take $p=3$ to reproduce the experimental probability distributions in Fig. 7 by means of Pearson type-III distribution,[22]

$$P(x;\sigma)=\frac{\sqrt{3}}{2\sigma}x^2\exp(-x)\,, \tag{3.1}$$

where $x=\sqrt{3}A/\sigma$. An analysis of the third moment of the distribution (related to its skewness) is consistent with this distribution (3.1). Its skewness is $2/\sqrt{3}\sim1.15$, comparable with the experimental values which fluctuate between 0.8 and 2.3 due to the instability inherent in estimating higher moments.[21] Although the asymmetry in our measurements could be related to the greater experimental difficulty in resolving the smaller particles, the skewness appears significant according to the estimate suggested in Ref. 21 [its value is ~20 times larger than its estimated Gaussian standard deviation $\sqrt{(6/N)}$]. The agreement between experimental and theoretical distribution is good, as can be seen in Fig. 7 [dotted lines are Eq. (3.1) multiplied by the respective histogram bin size].

C. Discussion on the activation energy

Two distinct activated processes may explain the observed size increase with substrate temperature: (i) a decreasing density of nuclei, and (ii) coalescence of smaller grains due to migration of material in the interstices. The former depends upon the nature of the substrate, and it should affect the earlier stages of growth when three-dimensional islands start to form.[8] In our experiment we probe aggregation after the first nucleation has been completed and coalescence occurs by migration of material to the interstitial regions between grains. The evolution of the grain-size distribution supports this, since growth of larger particles occurs at the expense of smaller ones. Under these conditions the growth is governed by diffusion,[24] in which case the 0.36-eV activation energy is identified with the corrugation of $T6$ surface potential to translational and angular motion of a $T6$ molecule or small cluster. The diffusional motion takes place until the migrating species finds a stable anchoring site and is captured, for instance, at the edge of a monolayer. This event leads to an increase in size of the aggregate, and the formation of a new anchoring site.

In the following, we try to support these arguments by studying the energetics of a $T6$ molecule (the probe) on an ordered $T6$ surface with a parametrization of the van der Waals (vdW) interactions. We calculate the minimum total interaction energy for different probe

orientations and adsorption sites, and we estimate the corrugation of the surface potential from differences between the energy minima.

In Fig. 9(a) we show the model for the interacting molecule and surface. The $T6$ molecules are rigid chains, each made of six identical spherical units. This approximation is convenient for implementing anisotropy in the attractive van der Waals forces and steric hindrance. However, each unit should not be regarded as an actual independent polarizable unit, due to the fact that additivity of individual electronic polarizations breaks down in large conjugated π systems.[25,26] The interaction between two units i and j on different molecules is calculated by the Lennard-Jones potential,

$$U_{ij}=4\varepsilon\left[\left[\frac{\rho}{r_{ij}}\right]^{12}-\left[\frac{\rho}{r_{ij}}\right]^{6}\right], \tag{3.2}$$

where r_{ij} is the distance between the centers of the two units. The two contributions in the potential (3.2) represent the repulsive and attractive interaction, respectively. Concerning the vdW diameter ρ, we take the equilibrium distance r_0 equal to the side-to-side nearest-neighbor distance in the solid (4.95 Å),[5] and use the well-known relation $r_0=2^{1/6}\rho$ (Ref. 25) to set $\rho=4.42$ Å. The energy parameter ε is set as described below. Among several shortcomings of this model are the neglect of important features in the molecular structure (dipoles, biaxiality, electrostatic interactions), surface structure (the herringbone packing of $T6$ molecules on the (100) surface [Fig. 9(b)]), and effect of surface disorder.

The model is parametrized using $T6$ single-crystal data.[5] Each monolayer is built with the monoclinic $P21/n$ lattice parameters: $b=7.85$ Å, $c=6.03$ Å, and a 23.5° tilt angle between the molecule and the a axis. A slab containing 2192 molecules arranged in eight stacked monolayers is used to represent the (100) surface [Fig. 9(a)]. The interaction energy U between the probe molecule and the surface is calculated by summing the individual contribution of each molecule in the surface. The packing energy of the crystal is estimated by summing the interactions between one molecule in the bulk and a large number of neighbors. This calculation was repeated

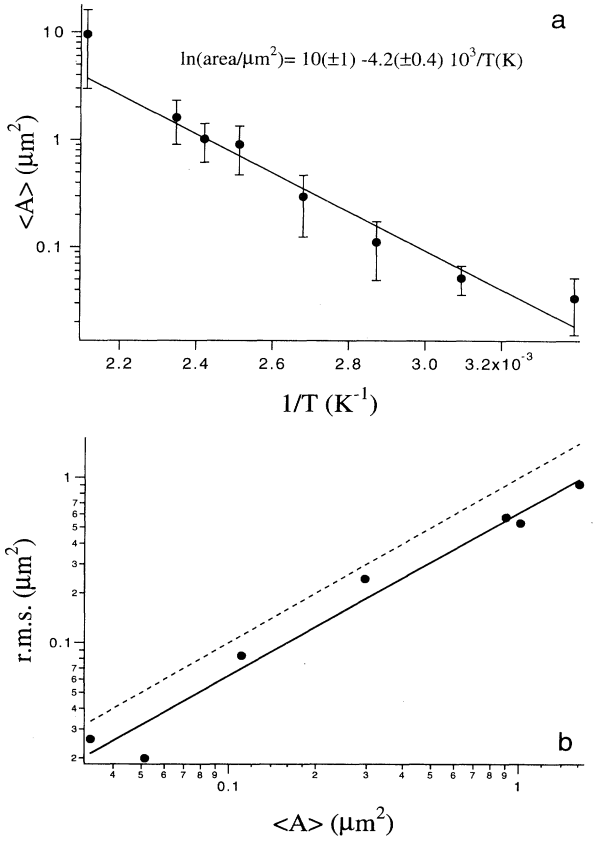

FIG. 8. (a) Plot of the average grain size vs inverse temperature. Error bars are estimated as average absolute deviation of the distribution, and inverse error bars are taken as statistical weights in least-square fitting. The best-fitting expression of the logarithmic area vs temperatures up to 150 °C is reported. Correlation coefficient is 0.985; (b) rms area fluctuation vs average grain size (circles). Continuous line is best fit of the double logarithm plot. Dotted line is the diagonal, as a reference to the eye.

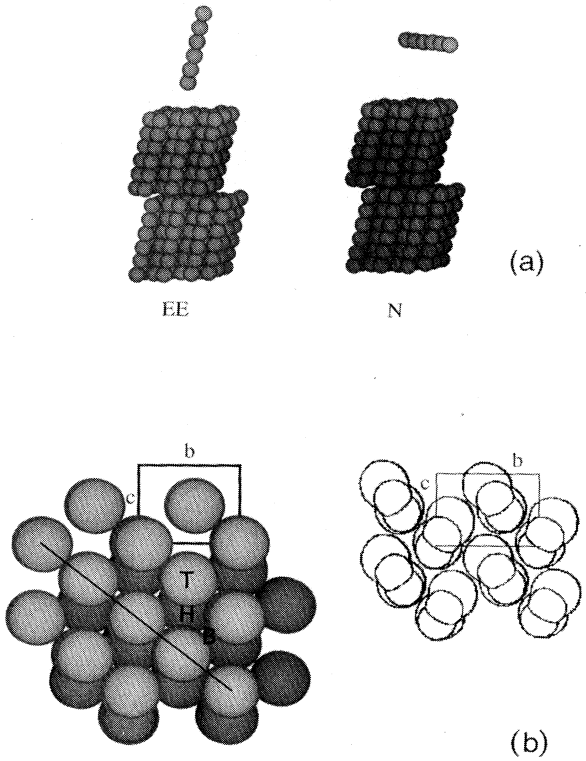

FIG. 9. Model for the calculation of the surface potential on a probe molecule. $T6$ is modeled as six spherical units, the surface as an eight-layer slab, and each layer consists of 266 molecules (only a part of the cluster is shown). (a) View of the two limit configurations: end-to-end (EE) and normal (N) configurations; (b) top view of the (100) surface from the model (left) and the crystal structure from Ref. 4 (right). The three relevant adsorption sites are marked T (top), B (bridge), and H (hollow). Solid straight line indicates the in-plane orientation of the molecular long axis in the N configuration.

for increasing cluster sizes until the packing energy converged to within about 0.01%.

In the actual solid there is an interpenetration between molecules in adjacent layers due to the small size of the end hydrogen atoms, whereas in our model the spherical shape of the end units prevents this due to excessive steric hindrance. Although the length of the molecule in the model (26.6 Å) matches the actual length (obtained by summing the XRD length of 24.4 Å and the vdW radii of the end hydrogen atoms, each 1.14 Å), using the real interlayer spacing for the a axis (22.35 Å) results in an unstable crystal. Therefore, we determined a suitable value for the a-axis parameter by minimization of the cluster packing energy, obtaining a larger (24.6 Å) interlayer spacing.

The energy parameter ε was evaluated by comparing the dimensionless packing energy with the results of more sophisticated calculations and desorption experiments (the desorption energy barrier is approximately the cohesive energy). For large cluster sizes the model packing energy converges to the value 72ε, and by comparison with the 2.7-eV packing energy reported previously,[27] ε is set as ~ 0.037 eV. This value of the packing energy is reasonable in light of the 2.13-eV desorption activation energy measured on $T5$ films,[8] considering that each additional thienyl unit contributes ~ 0.4 eV.[27] The binding energy between two molecules in a parallel side-to-side configuration (as adjacent neighbors in the crystal) is calculated to be $12\varepsilon \sim 0.44$ eV), which is in good agreement with experimental values on molecules (porphyrines) with a comparable number of π electrons (0.48 eV for 24 π electrons).[28]

The energetics are discussed using the two limit configurations shown in Fig. 9(a). They are termed end-to-end (EE) and normal (N) from the relative orientation of probe and surface molecule. In the EE configuration, the bottom thienyl unit of the probe is placed above top (T), bridge (B), or hollow (H) sites [indicated in Fig. 9(b)]. Similarly, in the N configuration the center of mass of the probe sits above the relevant sites. In the N configuration we have considered the most compact of the possible in-plane configurations, in which the probe molecule lies parallel to a row of nearest-neighbor surface units [shown as a straight line in Fig. 9(b)].

The laboratory x and y axes are taken to coincide with the crystallographic b-c axes [Fig. 9(b)], and the x-y plane cuts through the centers of mass of the uppermost units in the surface layer. The configurational variable z defines the height of the center of mass of the probe from the x-y plane. For each configuration the minimum energy is calculated as a function of z. The corrugation of the surface potential, hence the diffusional barrier, is calculated as the energy difference between local minima and the absolute minimum. The energy barrier to translation is given by the corrugation in a given configuration, whereas the barrier to rotation is given by the difference in energy between the EE and N configurations.

The total energy U/ε curves versus the configuration variable z for EE and N are plotted in Fig. 10. The N configuration [Fig. 10(b)] is energetically more stable (~ 0.97-eV binding energy) with respect to EE (~ 0.22 eV). Thus, an isolated molecule on the (100) surface will tend to lie flat rather than stand up. In the EE configuration $U_T > U_B > U_H$, and the energy differences are ~ 0.09 and 0.044 eV, respectively. In this case, we need to invoke a small cluster with few molecules at the interface to have a barrier comparable with the experimental value. In the N configuration $U_T \sim U_B > U_H$ and the corrugation of the surface potential is ~ 0.27 eV. At a kink site, for instance at the edge of a monolayer, the molecule in the N configuration needs to reorient to EE in order to be adsorbed on the (012) surface. Although our model does not apply to the edge of the surface, we can estimate the lowest energy required to rotate from the N to EE configuration (from the T position in N to the H position in EE) to be about 0.5 eV.

Our simple model suggests, albeit without proving, that two diffusional barriers that might be relevant to $T6$ film growth, translation of a molecule in the N configuration across the surface (0.27 eV), and reorientation of the molecule from the N to the EE configuration (0.5 eV), are both comparable to the observed value 0.36 eV.

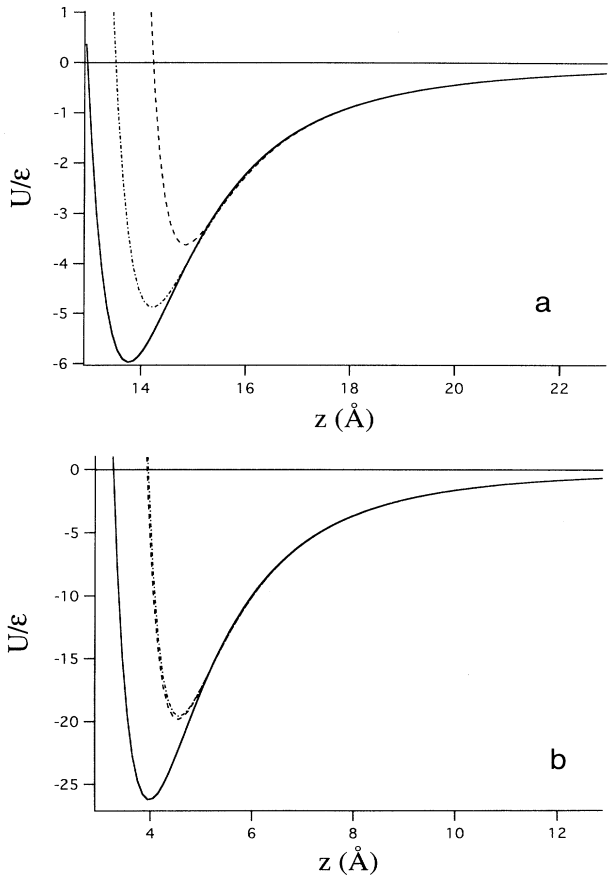

FIG. 10. Dimensionless interaction potential between a probe molecule and the (100) surface in the (a) end-to-end and (b) normal configurations. The abscissa z is the distance between the reference x-y plane (see text) and the probe center of mass. The curves correspond to the probe center of mass above top (dashed line), bridge (dashed-dotted), and hollow (solid) sites.

IV. CONCLUDING REMARKS

We have performed a quantitative AFM study of the effect of the substrate temperature during the evaporation on the growth of a molecular thin film of sexithienyl on mica. The conditions we used for deposition are close to those used for preparing a $T6$ active layer for LED devices (thickness ~ 100 nm). The parameters we fixed in the experiment are the evaporation rates (between 0.2 and 1 Å/s), the thickness, and the substrate.

We have shown how the temperature of the substrate during the evaporation is an effective parameter for systematic control of $T6$ film morphology in terms of grain size and aggregation phase. This is relevant to the physical properties of the system, such as carrier mobility and optical polarization, and can be exploited to tailor the properties of the film. Properties of $T6$ films prepared above 200 °C are yet to be measured, but our observations suggest that anisotropy and long-range-order effects will be enhanced further.

In order to access statistical information on the growth process, we have used AFM to collect a large number of images of each sample, and selected the representative results by means of a comparison of the power spectra. We have shown that scanning probe microscopies are convenient not only for nondestructive investigations, but also to assess the reproducibility of sample features.

The central result of the present work is that measurement of nanometer-to-micrometer scale features with AFM can be used to acquire information on mechanistic properties relevant to the growth process which are not easily accessible for surface phenomena, such as activation energy. They can be measured with 10–20 % accuracy from the analysis of several hundred particles. Such information is valuable for designing new multilayer structures, and can be useful for modeling growth properties and interface evolution. The activated increase in grain size, and the skewed particle size distribution are consistent with a process of coalescence between smaller particles, which depends on the mobility of molecules or small clusters. A diffusion-controlled growth is intuitively in agreement with the intrinsic low mobility of $T6$ molecules, arising from the presence of highly polarizable π electrons and a large mass. We have shown with a simple model that there the experimental value (0.36 ± 0.04 eV) is comparable to possible diffusional (translational and rotational) barriers for a single $T6$ molecule on a $T6$ surface (0.3–0.5 eV). Although the good agreement is probably fortuitous, it encourages the analysis of AFM data on a wide range of spatial lengths with more rigorous models in order to elucidate the microscopic growth mechanism of organic thin films.

ACKNOWLEDGMENTS

We are grateful to R. N. Marks, V. Palermo, C. Zannoni, P. Guptasarma, P. Ruani, V. M. Kenkre, M. Möller, and S. Sheiko for useful suggestions and discussions, and G. Calestani for helping us with crystal modeling. R. Danieli and S. Rossini have synthesized $T6$. We also thank ASSING-SpA for technical support. F.B. would like to thank INFM for financial support. Partial funding for this work was provided by EEC research programs Esprit Basic Research 8013 LEDFOS and Human Capital and Mobility Network SELMAT, and Progetto Strategico Materiali Innovativi-CNR.

*Present address: Dipartimento Chimica Fisica ed Inorganica, Universitá di Bologna, Viale Risorgimento 4, 40136 Bologna, Italy.

[1](a) G. Horowitz, X. Peng, D. Fichou, and F. Garnier, J. Appl. Phys. **67**, 528 (1990); (b) G. Grem, G. Leditzky, B. Ulrich, and G. Leising, Adv. Mater. **4**, 36 (1992); (c) H. Akimichi, K. Waragai, S. Hotta, H. Kano, and H. Sakaki, Appl. Phys. Lett. **58**, 1500 (1991); (d) P. Ostoja, S. Guerri, S. Rossini, M. Servidori, C. Taliani, and R. Zamboni, Synth. Met. **54**, 447 (1993); (e) A. Dodabalapur, L. Torsi, and H. E. Katz, Science **268**, 270 (1995).

[2]J. H. Burroughes, D. D. C. Bradley, A. R. Brown, R. N. Marks, K. Mackay, R. H. Friend, P. L. Burns, and A. B. Holmes, Nature **347**, 539 (1990); D. Braun and A. J. Heeger, Appl. Phys. Lett. **58**, 1982 (1991).

[3](a) N. Periasamy, R. Danieli, G. Ruani, R. Zamboni, and C. Taliani, Phys. Rev. Lett. **68**, 919 (1992); (b) O. Dippel, V. Brandl, H. Bässler, R. Danieli, R. Zamboni, and C. Taliani, Chem. Phys. Lett. **216**, 418 (1993); (c) H.-J. Egelhaaf, P. Bäuerle, K. Rauer, V. Hoffmann, and D. Oelkrug, Synth. Met. **61**, 143 (1993); (d) D. Oelkrug, H.-J. Egelhaaf, D. R. Worrall, and F. Wilkinson, J. Fluorescence **5**, 165 (1995); (e) for a review, see S. Hotta and K. Waragai, Adv. Mater. **5**, 896 (1993).

[4]W. Porzio, S. Destri, M. Mascherpa, and S. Brückner, Acta Polymer. **44**, 266 (1993).

[5]G. Horowitz, B. Bachet, A. Yassar, P. Lang, F. Demanze, J-L. Fave, and F. Garnier, Chem. Mater. **7**, 7 (1995).

[6]B. Servet, S. Ries, M. Trotel, P. Alnot, G. Horowitz, and F. Garnier, Adv. Mater. **5**, 461 (1993).

[7]B. Servet, G. Horowitz, S. Ries, O. Lagorsse, P. Alnot, A. Yassar, F. Deloffre, P. Srivastava, R. Hajlaoui, P. Lang, and F. Garnier, Chem. Mater. **6**, 1809 (1994).

[8]O. Böhme, C. Ziegler, and W. Göpel, Synth. Met. **67**, 87 (1994).

[9]K. Hamano, T. Kurata, S. Kubota, and H. Koezuka, Jpn. J. Appl. Phys. **33**, L1031 (1994).

[10]M. Buongiorno Nardelli, D. Cvetko, V. De Renzi, L. Floreano, R. Gotter, A. Morgante, M. Peloi, F. Tommasini, R. Danieli, S. Rossini, C. Taliani, and R. Zamboni (unpublished).

[11]A. Stabel and J. P. Rabe, Synth. Met. **67**, 47 (1994); P. Bäuerle, T. Fischer, B. Bidlingmeier, A. Stabel, and J. P. Rabe, Angew. Chem. Int. Ed. Engl. **34**, 303 (1995).

[12]G. Lanzani, L. Rossi, A. Piaggi, A. J. Pal, and C. Taliani, Chem. Phys. Lett. **226**, 547 (1994).

[13]L. M. Blinov, S. P. Palto, G. Ruani, C. Taliani, A. A. Tevosov, S. G. Yudin, and R. Zamboni, Chem. Phys. Lett. **232**, 401 (1995).

[14]M. Pope and C. E. Swemberg, *Electronic Processes in Organic*

Crystals (Clarendon, Oxford, 1982).
[15]P. Ostoja, S. Guerri, M. Impronta, P. Zabberoni, R. Danieli, S. Rossini, C. Taliani, and R. Zamboni, Adv. Mater. Opt. Electron. **1**, 127 (1992).
[16]R. N. Marks, F. Biscarini, R. Zamboni, and C. Taliani, Europhys. Lett. (to be published).
[17]C. Taliani, R. Zamboni, G. Ruani, S. Rossini, and R. Lazzaroni, J. Mol. Electron. **6**, 225 (1990); S. Destri, M. Mascherpa, and W. Porzio, Adv. Mater. **5**, 43 (1993).
[18]R. P. Van Duyne, J. C. Hulteen, and D. A. Treichel, J. Chem. Phys. **99**, 2101 (1993).
[19]Ph. Dumas, B. Bouffakhreddine, C. Amra, O. Vatel, E. Andre, R. Galindo, and F. Salvan, Europhys. Lett. **22**, 717 (1993).
[20]D. J. Keller, Surf. Sci. **253**, 353 (1991).
[21]W. H. Press, B. P. Flannery, S. A. Teukolsky, and W. T. Vetterling, *Numerical Recipes: The Art of Scientific Computing* (Cambridge University Press, Cambridge, 1990).
[22]M. Abramowitz and I. Stegun, *Handbook of Mathematics* (Dover, New York, 1972).
[23]N. G. Van Kempen, *Stochastic Processes in Physics and Chemistry* (Elsevier, Amsterdam, 1981).
[24]K. L. Chopra, *Thin Film Phenomena* (McGraw-Hill, New York, 1969).
[25]J. Israelachvili, *Intermolecular and Surface Forces* (Academic, San Diego, 1992).
[26]M. T. Zhao, B. P. Singh, and P. N. Prasad, J. Chem. Phys. **89**, 5535 (1988).
[27]A. Gavezzotti and G. Filippini, Synth. Met. **40**, 257 (1991).
[28]C. A. Hunter and J. K. M. Sanders, J. Am. Chem. Soc. **112**, 5525 (1990).

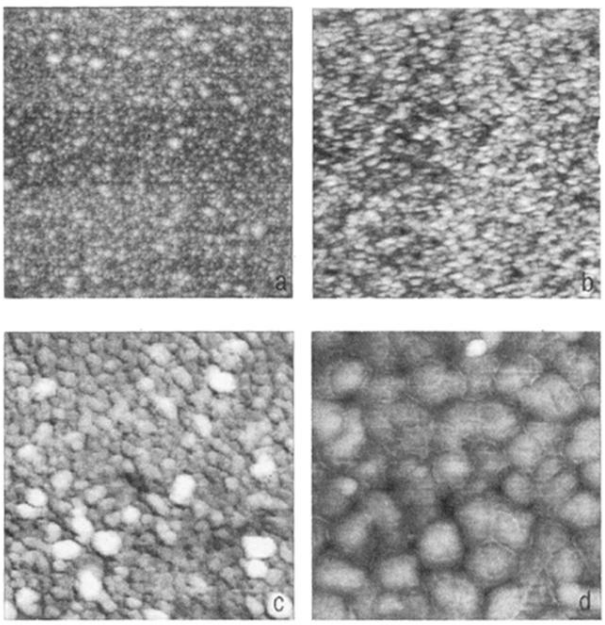

FIG. 2. 10 μm $\times$ 10 μm unfiltered topographical images of $T6$ films evaporated on mica. Substrate temperatures are (a) 22 °C (vertical scale 0–102 nm, scan rate 5 Hz); (b) 75 °C (vertical scale 0–130 nm, scan rate 3 Hz); (c) 100 °C (vertical scale 0–102 nm, scan rate 5 Hz); (d) 150 °C (vertical scale 0–132 nm, scan rate 10 Hz). Resolution is 400 pixels per line.

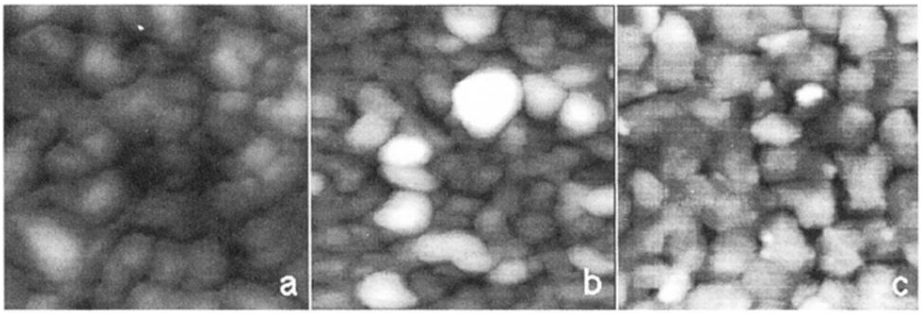

FIG. 3. Unfiltered topographical images of $T6$ films showing the similar morphology for samples evaporated on mica at (a) 22 °C (1-μm × 1-μm zoom from a 2-μm × 2-μm image); (b) 100 °C (5 μm × 5 μm); (c) 150 °C (10 μm × 10 μm).

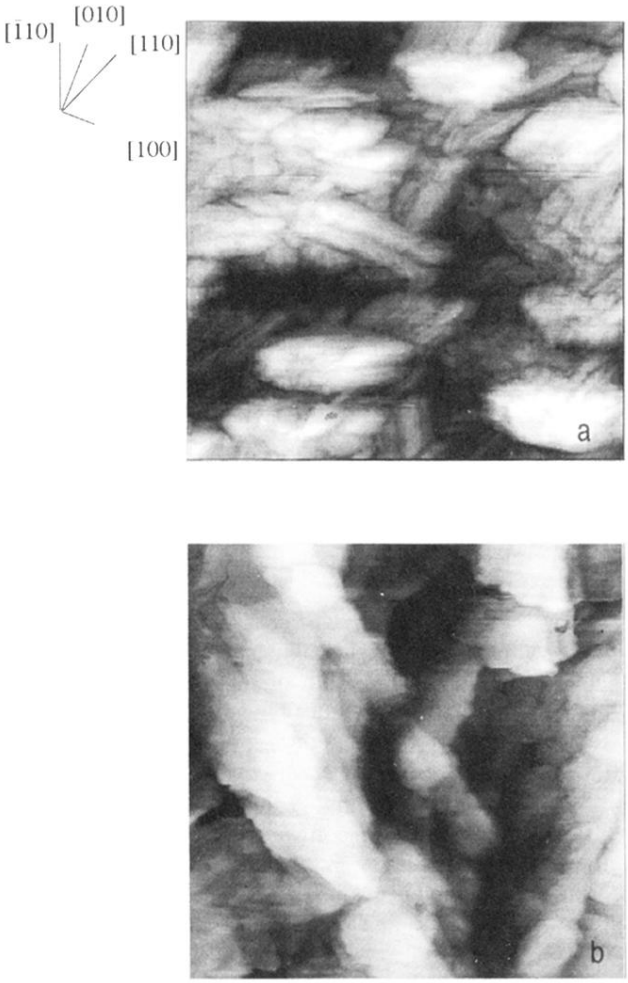

FIG. 4. 10-μm$\times$10-μm topographical images of $T6$ films evaporated on mica at (a) 200 °C (scale bar 0–346 nm, scan rate 5 Hz) and (b) 220 °C (scale bar 0–880 nm, scan rate 5 Hz). Solid lines show the preferred orientation of the crystallites. Labels correspond to possible mica lattice directions. The contrast is enhanced by equalization of the histogram.

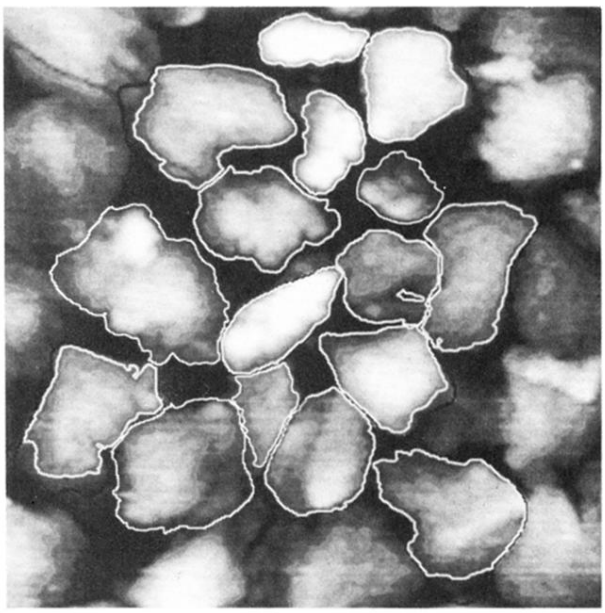

FIG. 5. Sampling of projections for the statistics of grain size. Solid black lines follow the major crevices and necks around each grain; white line is the contour selected by thresholding. The area is calculated from pixel-by-pixel counting within the white line.

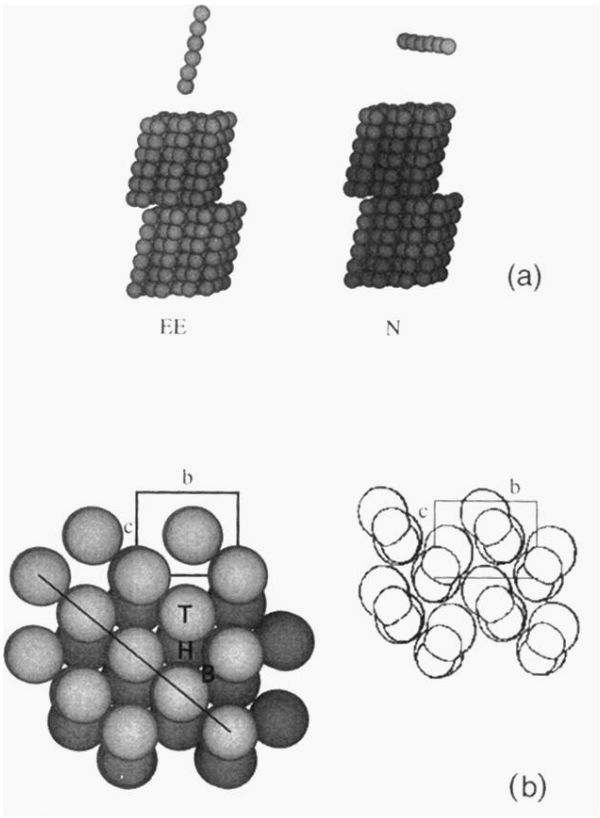

FIG. 9. Model for the calculation of the surface potential on a probe molecule. $T6$ is modeled as six spherical units, the surface as an eight-layer slab, and each layer consists of 266 molecules (only a part of the cluster is shown). (a) View of the two limit configurations: end-to-end (EE) and normal (N) configurations; (b) top view of the (100) surface from the model (left) and the crystal structure from Ref. 4 (right). The three relevant adsorption sites are marked T (top), B (bridge), and H (hollow). Solid straight line indicates the in-plane orientation of the molecular long axis in the N configuration.